Authigenic uranium isotopes of late Proterozoic black shale

D. H. Dang[1,2,3*], W. Wang[1], T. M. Gibson[4], M. Kunzmann[5**],
M. Andersen[6], G. P. Halverson[7], R. D. Evans[1,3]

Affiliations:

[1]School of the Environment, Trent University, Peterborough, Canada.

[2]Department of Chemistry, Trent University, Peterborough, Canada.

[3]Water Quality Center, Trent University, Peterborough, Canada.

[4]Department of Earth & Planetary Sciences, Yale University, New Haven, USA

[5]CSIRO Mineral Resources, Australian Resources Research Centre, Kensington, Australia.

[6]School of Earth and Environmental Sciences, Cardiff University, Cardiff, UK.

[7]Department of Earth & Planetary Sciences and Geotop, McGill University, Montreal, Canada.

*Corresponding author: huydang@trentu.ca

** Current address: Fortescue Metals Group Ltd., East Perth, WA 6004, Australia

Abstract: The evolution of early life is intimately related to environmental changes on Earth, and in particular, the accumulation of oxygen in the atmosphere and oceans. However, the record of environmental O_2 abundance in the middle to late Proterozoic Eon, during which many new eukaryotic lineages emerged, is sparse and controversial. Here we present a uranium (U) isotope record from late Proterozoic shales from northwestern Canada, Arctic Canada (Baffin Island), Svalbard, and Greenland, coupled with a novel approach for inferring authigenic U isotope values ($\delta^{238}U_{authigenic}$). A compilation comprising our new data and available literature data (854 $\delta^{238}U_{authigenic}$ values) through geologic time indicates a consistent rise in $\delta^{238}U_{authigenic}$ values following the Great Oxidation Event. This gradual increase in $\delta^{238}U$ can be interpreted as an increase in the frequency of transient oxygenation events and also as a variation of U isotope fractionation factors between authigenic uptake and seawater ($\Delta^{238}U$) associated with different redox conditions occurring over the Earth's history. In conjunction with the U isotopic signature, we used previously published Fe speciation data from our samples to infer local controls on U incorporation and isotopic fractionation. The results suggest that late Proterozoic oceans were dominantly ferruginous, punctuated by periods of transient oxygenation. During these transient oxic conditions, high U isotope fractionation resulted in $\Delta^{238}U$ values as high as ~1.2 ‰ relative to the $\delta^{238}U_{crust}$. However, under ferruginous conditions, smaller isotopic fractionation led to $\Delta^{238}U$ values <0.6 ‰. Integrating conclusions from our study with other geochemical studies suggests the occurrence of several spatially localized oxygenation events across the globe during the late Proterozoic. These conclusions help to better integrate geochemical and fossil records in the context of early evolution of complex life.

Keywords: U isotopes; Proterozoic; black shale; oxygenation; paleo-redox

1. Introduction

Geochemical evidence suggests that the Earth's atmosphere remained largely oxygen-free until the Great Oxidation Event (GOE) ca. 2.4 Ga, when O_2 levels first exceeded ~0.001% of present atmospheric levels (PAL, Lyons et al., 2014; Gumsley et al., 2017). The GOE dramatically impacted biogeochemical processes and the evolutionary trajectory of early life (Butterfield, 2009; Lyons et al., 2014; Smit and Mezger, 2017). There is growing consensus that atmospheric oxygen levels rose dramatically in the early Paleoproterozoic Era, perhaps approaching modern levels, and subsequently crashed ca. 2.0 Ga following the ca. 2.3–2.1 Ga Lomagundi-Jatuli positive carbon isotope excursion (Hodgskiss et al., 2019; Mänd et al., 2020). Multiple independent redox-sensitive proxies suggest oxygen levels then remained low through the following billion years during the middle Proterozoic Eon, although these levels are both poorly constrained and contentious (Partin et al., 2013; Planavsky et al., 2014; Crockford et al., 2018).

A second, late Proterozoic oxygenation event has long been inferred, in part based on the appearance of Metazoa (Planavsky et al., 2014; Cole et al., 2020a). Although also controversial, this Neoproterozoic oxygenation event (NOE) is supported by diverse datasets, notably Cr, Mo and S isotopes in organic-rich shale records (e.g., Kendall et al., 2015; Cole et al., 2016; Kunzmann et al., 2017a). However, other datasets suggest that oxygenation was more protracted and even largely delayed until the early (Sperling et al., 2015) or even middle Paleozoic Era (Dahl et al., 2010; Wallace et al., 2017; Krause et al., 2018). Furthermore, spatial and temporal patterns of the NOE remain nebulous at best (Kunzmann et al., 2017b), plagued by poorly age-calibrated and often discontinuous records, along with the intrinsically limited quantitative information provided by most geochemical redox proxies. Discrepancies between geochemical data, the metazoan fossil record, and molecular clock estimates further complicate this history (Erwin et al., 2011; Cole et al., 2016; Sahoo et al., 2016; Cheng et al., 2018). The argument that late Neoproterozoic to early Paleozoic oxygenation was a consequence rather than prerequisite of the early animal evolution has gained traction (Butterfield, 2009; Lenton et al., 2014). The redox dynamics of the late Proterozoic oceans also remain controversial. There is strong evidence for both regionally anoxic conditions until at least the Ediacaran Period (Sperling et al., 2015; Cheng et al., 2018) and also discrete oxygenation events (Sahoo et al., 2016). Thus, the presence of stable anoxic conditions at

this time is unlikely, and instability may have contributed to metazoan radiation through morphological evolution and novelty (Wood and Erwin, 2018; Cole et al., 2020a).

Constraining when oxygen concentrations were sufficiently high to facilitate the energy-expensive and O_2-demanding lifestyles of complex animals (e.g., motility and predation) is critical for disentangling the causal relationship between global oxygenation and metazoan evolution (Narbonne, 2004; Xiao and Laflamme, 2009; Sperling et al., 2013; Mills et al., 2014; Sahoo et al., 2016). Mills et al. (2014) demonstrated that simple metazoans can survive in as little as 4% PAL pO_2 (Mills et al., 2014). Other recent studies have demonstrated U isotope fractionation in Mesoarchean shallow marine and continental shale (3.07-2.0 Ga) associated with biological production (Wang et al., 2020). This finding suggests a mildly oxidative weathering regime at Earth's surface by 3.0 Ga. Trace elements and Mo isotopes in ca 2.2 Ga Mn oxide deposits imply extensive deposition of oxides under oxidizing marine conditions with O_2 concentration above 10 µM (Goto et al., 2021). Other trace metal, biomarker and Cr isotope datasets suggest that pO_2 of at least >1% PAL were achieved, at least transiently, between 1.4 Ga and 1.1 Ga (Gilleaudeau et al., 2016; Zhang et al., 2016; Canfield et al., 2018). At ca. 1.4 Ga, pO_2 was estimated to be at least 1% and possibly as high as 9% PAL (Canfield et al., 2018; Liu et al., 2020; Wei et al., 2021). However, several lines of evidence, including Cr isotope ratios in marine shale, imply extremely low pO_2 (<0.1% PAL) until ca. 0.8 Ga (Planavsky et al., 2014; Cole et al., 2016). These seemingly incompatible results raise the possibility that the history of late Proterozoic oxygenation was not one of simple monotonic rise, but rather fluctuations superimposed upon a longer, protracted increase through time. Therefore, a better understanding of the oxygenation history of the late Proterozoic will help to integrate geochemical and fossil records in the context of animal evolution.

In this light, we investigated a collection of marine shales spanning the Neoproterozoic Era during which the Earth's ancient landscape underwent important redox, climatic, and biological transitions. The shale samples span from ca. 1.05 to 0.63 Ga and are derived from northwestern Canada (0.95-0.62 Ga), Baffin Island (ca. 1.05 Ga), Greenland (0.66-0.655 Ga), and Svalbard (0.80-0.63 Ga) (**Fig. S1**). Here, we report the concentrations of redox-sensitive elements (U, Mo) and U isotope data (see section 2.1) to constrain the redox conditions of the depositional environments. In order to isolate the authigenic U signature in these shales (see section 2.2), we

developed a sample leaching protocol. This procedure is essential for these samples because siliciclastic samples can have a high proportion of detrital U relative to their authigenic component. In conjunction with the U isotopic signature of these samples, we used previously published Fe speciation data (Kunzmann et al., 2017b; Gibson et al., 2020; Hodgskiss et al., 2020) to infer local controls on U incorporation and isotopic fractionation in these shale.

2. Background

2.1.The U isotope paleo-redox proxy

Uranium, a redox-sensitive element (RSE), and its isotopes have emerged as useful tools for ocean paleo-redox reconstructions. Although the two most common U isotopes (^{238}U and ^{235}U) are radioactive, their half-lives are relatively long (~4.5 and 0.7 Ga, respectively; Jaffey et al., 1971). Thus, U isotope fractionations that involve non-radioactive processes leading to U isotope exchange are recorded as variations in $^{238}U/^{235}U$ ratios (Andersen et al., 2017), which are widely reported in δ-notation (i.e., $\delta^{238}U$, Eq. 1).

$$\delta^{238}U\ (‰) = \left[\frac{\left(\frac{^{238}U}{^{235}U}\right)_{sample}}{\left(\frac{^{238}U}{^{235}U}\right)_{IRMM-184}} - 1\right] \times 10^3 \quad (Eq.\ 1)$$

Specifically, the application of U isotope systematics as a paleo-redox proxy primarily relies on significant isotope fractionation during U reduction (Stirling et al., 2007; Weyer et al., 2008). The U isotopic shifts are associated with the nuclear field shift effect arising from the variations of nuclear volume and electron density distributions between isotopes. This effect is particularly significant for elements with heavy masses with large nuclei like uranium (Stirling et al., 2015 and references therein).

Uranium has two primary oxidation states: soluble U^{VI} and insoluble U^{IV}; the latter is responsible for U removal from seawater in reducing environments (Barnes and Cochran, 1990). Laboratory studies have shown that the reductive accumulation of U^{IV} induces U isotopic fractionation ($\Delta^{238}U = \delta^{238}U_{red} - \delta^{238}U_{ox}$) up to 1.2 ‰ (Stylo et al., 2015; Dang et al., 2016). Therefore, heavy ^{238}U is preferentially removed from the water column during reductive accumulation in sediment, driving the remaining reservoir isotopically lighter (Stylo et al., 2015; Dang et al., 2016). However, major

challenges in interpreting Earth's redox history using U isotopes persist, including differentiating between local and global signals (Lyons et al., 2009) and estimating U isotope fractionation in different redox environments.

In modern oceans which are predominantly oxic, significant U isotope fractionation occurs in sediment that underlies reducing bottom waters (e.g., Stirling et al., 2007; Weyer et al., 2008; Andersen et al., 2017). These reduced environments represent the largest oceanic U sink (Dunk et al., 2002) and therefore function as the main lever controlling the global marine U isotope mass balance. Therefore, although the U isotope composition is variable in reduced environments (Andersen et al., 2017), it is on the whole enriched in ^{238}U relative to seawater, which itself is reciprocally depleted relative to average upper continental crust (i.e., $\delta^{238}U$ = -0.31±0.14 ‰; Kendall et al., 2013). Extrapolating this understanding of the mechanisms leading to U enrichment and isotope fractionation systematics allows U isotopes in ancient sediment to be used as a paleo-redox proxy that can track the redox evolution of ancient environments (Kendall et al., 2015; Lau et al., 2017; Yang et al., 2017). However, recent studies have questioned the applicability of modern U isotope systematics to paleo-environments due to the variable U isotope fractionation experienced under different depositional conditions (Cole et al., 2020b), as well as variable U ocean residence and ocean mixing times over Earth's history (Chen et al., 2021).

Black shale and carbonate rocks are the two most targeted geological archives for measuring U isotopes as they are the two major oceanic sinks for U (Andersen et al., 2016). In most modern oxygenated environments, the U isotopic composition in carbonate approximates seawater because the structural incorporation of $UO_2(CO_3)_3^{4-}$ results in limited isotope fractionation ($\Delta^{238}U_{carb}$ <0.2 ‰; Andersen et al., 2017). However, it remains unclear how syn- and post-depositional diagenetic processes alters the primary U isotopic signal in carbonate (Romaniello et al., 2013; Zhang et al., 2020). Therefore, the interpretation of seawater U isotopic composition from carbonate rocks requires complementary indicators for diagenetic processes (e.g., stable isotopes, Mn/Sr, Mg/Ca ratios) and consideration of carbonate mineralogy to exclude post-depositional alteration (Lau et al., 2017). On the other hand, although U isotopes are fractionated at variable degrees during incorporation into organic-rich shale ($\Delta^{238}U$ ~ 0.3 to 1.0 ‰; Andersen et al., 2017), this archive

still records the changing oxidation state of seawater and is intrinsically less susceptible to alteration by fluid flow than in carbonate.

In modern environments, the high $\Delta^{238}U$ expressed during U incorporation into organic-rich muds is a consequence of the partial U^{VI}-to-U^{IV} reduction under anoxic conditions. As such, high $\delta^{238}U$ in organic-rich shale could be an indicator of increasing atmospheric and oceanic O_2 levels and U^{VI} mobilization and transport to the ocean due to oxidative weathering, at least at a localized scale (Andersen et al., 2017). However, a major caveat is that organic-rich muds deposited under differing redox conditions fractionate U isotope values to different extents, which requires further scrutiny (Andersen et al., 2020). Irrespectively, within such a framework, high $\delta^{238}U$, relative to the continental crust (-0.3 ‰), in ancient organic-rich shale from the Mesoarchean (Wang et al., 2018) and at 2.5 Ga, 1.98 Ga, 1.36 Ga, 0.66 Ga, and 0.56 Ga, have been interpreted as a record of discrete oceanic oxygenation events (Kendall et al., 2013; Kendall et al., 2015; Yang et al., 2017; Mänd et al., 2020). However, more recent studies have demonstrated that U isotopes in both shale and carbonate facies deposited under ferruginous conditions were highly variable, but with a muted U isotope fractionation on average (~ + 0.1 ‰, which is similar to oxic sinks) (Cole et al., 2020b; Chen et al., 2021).

Another important consideration in interpreting U concentrations and isotopic data in ancient depositional settings is the reservoir they are tracking (e.g., local, regional, or global water masses). The conservative behavior of the dominant U^{VI} seawater species, the uranyl carbonate ion (Henderson and Anderson, 2003), leads to long oceanic residence times of U in modern oxygenated oceans (ca. 400-500 kyr, Henderson and Anderson, 2003) which are well-mixed, resulting in a globally uniform U isotopic signal ($\delta\ ^{238}U$ ~ -0.39 ‰, Andersen et al., 2017). Therefore, it has been suggested that U isotopes can be used as a global redox proxy (Weyer et al., 2008). However, the oceanic residence time of U in the anoxic Archean ocean may have been orders of magnitude shorter due to the dominance of particle reactive U^{IV} (Partin et al., 2013) and a larger marine U sink from increased anoxic coverage of the seafloor area (Chen et al., 2021). The fact that U ocean residence time may have been close to the ocean mixing timescale (0.1 to 10 kyr) in the Precambrian makes U isotope systematics likely to reflect local/regional redox conditions rather than global oceanic conditions (Partin et al., 2013; Chen et al., 2021).

2.2.Authigenic uranium isotope compositions and redox reconstruction

The widespread use of trace elements (notably the RSEs) in marine shale as a redox proxy in paleo-environmental studies requires an accurate differentiation between detrital (transported or particulate) and authigenic fractions (precipitated from seawater). It is often assumed that the authigenic fraction of an element in a solid sample can be approximated by the difference between bulk concentration (whole-rock digestion) and the detrital fraction (i.e., $[U_{authigenic}]=[U_{bulk}]-[U_{detrital}]$) (Xu et al., 2012; Wang et al., 2020). The latter is often calculated from a fixed detrital RSE/Al ratio (i.e., $[U_{detrital}]=[Al] \times U/Al_{detrital}$). Traditionally, a single crustal average is used to represent the detrital input, e.g., U/Al ratio of 0.33 (ppm/wt%), but these values can be significantly offset from the continental weathering source (0.58±1.1 ppm/wt% in top soils from 4,850 localities; Cole et al., 2017). Via isotopic mass balance, the $\delta^{238}U_{authigenic}$ values can be, therefore, calculated from the difference between the U concentration and isotope composition in the whole-rock digestion (bulk, measured) and detrital (computed):

$$\delta^{238}U_{authigenic} = \frac{[U_{bulk}] \times \delta^{238}U_{bulk} - [U_{detrital}] \times \delta^{238}U_{detrital}}{[U_{authigenic}]} \quad (Eq.2)$$

In reality, the heterogeneity in the nature of particulate materials which ultimately make up detrital sediment, and effects of physical and chemical weathering on these particles, requires either a precise reevaluation of the traditional detrital elemental ratio and U isotope composition (i.e., $U/Al_{detrital}$ or U/Th) (Cole et al., 2017), or an alternative method for assessing the detrital fraction, such as a selective digestion method. One selective leaching approach that has been previously applied to Triassic and Permian black shale from Svalbard, Svalis Dome, the Norwegian shelf and East Greenland uses *aqua regia* to assess the authigenic contribution in marine shale (Xu et al., 2012). Another study uses concentrated nitric acid (15 M) to leach shale powder to dissolve the authigenic component (Wang et al., 2020). The *aqua regia* or concentrated acid leach primarily releases trace metals reflecting the hydrogenous "seawater" component, e.g., those bound to organic matter, sulfide and carbonate minerals, while the detrital fraction composed mainly of silicate minerals remains largely unaffected (Xu et al., 2012). Therefore, U concentrations and isotope compositions analyzed in such leachates could be directly attributed to the authigenic fractions. In this case, the detrital $\delta^{238}U$ can be calculated from the difference between the U

concentration and isotope composition in the whole-rock digestion (bulk) and leachates (authigenic) (Eq. 3). The most important advantage of this approach is that all variables are measured instead of being computed based on a theoretical assumption, which minimizes uncertainty of the U isotope composition.

$$\delta^{238}U_{detrital} = \frac{[U_{bulk}] \times \delta^{238}U_{bulk} - [U_{authigenic}] \times \delta^{238}U_{authigenic}}{[U_{detrital}]} \quad (Eq. 3)$$

To summarize, the reliable extraction of authigenic signatures requires careful scrutiny for obtaining environmental redox information. This is particularly true for the shale records because of a mixture of detrital and authigenic fractions. For ancient samples where authigenic U and RSE enrichment may be low (Yang et al., 2017), the bulk $\delta^{238}U$ may be dominated by the detrital fraction, which is expected to approximate bulk upper continental crustal compositions. Thus, for samples with low authigenic U, it is essential to reliably separate the authigenic from the detrital signatures. The former is necessary to better constrain U isotope ocean mass balance and the mechanisms of U isotope fractionation under various specific redox conditions relevant to ancient marine environments (e.g., oxic, ferruginous, sulfidic). Although shale $\delta^{238}U$ data exist for discrete intervals throughout the Proterozoic Eon (Kendall et al., 2013; Kendall et al., 2015; Lau et al., 2017; Yang et al., 2017), data coverage from the critical interval 1.05–0.66 Ga, during which eukaryotes diversified (Knoll, 2014), is sparse.

3. Materials and Methods

3.1.Geological and geochemical settings

Dark grey to black shale assessed in this study were collected from northwestern Canada (n = 50), Baffin Island (n = 34), Greenland (n = 7) and Svalbard (n = 43). Many of these samples were used and described in prior studies (Kunzmann et al., 2017a, b; Gibson et al., 2020; Hodgskiss et al., 2020). A summary of the stratigraphic units, including their age, comprising the sampled sections is given in Table S1, together with references that provide detailed geological descriptions.

Northwestern Canada: Six sections (M103, M106, G23, G0233, T1515, T1527) come from early Tonian (ca. 920-800 Ma) and early Ediacaran (ca. 630-620 Ma) stratigraphic units in Yukon and Northwest Territories. Most of these shale are characterized by low Fe_{HR}/Fe_T (<0.38) and a lack

of enrichment in RSEs (Sperling et al., 2013; Kunzmann et al., 2017b; Gibson et al. 2020), indicating oxygenated surface layers likely overlying deeper anoxic waters. Samples from sections T1515 and T1527 are from Aok Formation (ca. 900 Ma) and Mikkelson Islands Formation (ca. 950 Ma), of the Shaler Supergroup in the Brock Inlier (Van Acken et al., 2013). Further description of other samples is provided elsewhere (Kunzmann et al., 2017b).

Baffin Island: Four sections (T1510, T1413, T1412, G1431) were sampled from different formations of the late Mesoproterozoic Bylot Supergroup, which overlies basalts thought to correspond to the 1.27 Ga Mackenzie large igneous province. Section T1413 is from the Arctic Bay Formation, T1412 is from the Iqqittuq Formation, and G1431 is from the Victor Bay Formation. These units are ca. 1.050 Ga based on Re-Os dates on the upper Arctic Bay and lower Victor Bay formations ((Gibson et al., 2018). Section T1510 is from the Sinasiuvik Formation, at the top of the Bylot Supergroup, which is likely ca. 1.0 Ga (Gibson et al., 2019). This succession also preserves the fossil *Bangiomorpha pubescens*, widely regarded as the oldest crown group (red) alga (Butterfield, 2000). Also, it is important to note that depositional environments within the Borden Basin fluctuated between marine and either lacustrine or restricted marine. Further details are provided by Gibson et al. (2018, 2019) and Hodgskiss et al. (2020).

Greenland: The section GR12 constitutes the lower part of the Cryogenian interglacial Arena Formation. This section is equivalent to the Macdonaldryggen Member in Svalbard, with ages of ca. 660-655 Ma (Halverson et al., 2018). Fe_{HR}/Fe_T ratios in this section span from 0.2 to 0.8, but most of the data fall in a range that does not allow clear distinction between oxic and anoxic conditions. Further descriptions are provided by Kunzmann et al. (2017b).

Svalbard: The Neoproterozoic succession in Svalbard is one of the most complete records of the Tonian and Cryogenian periods, recording both the Sturtian and Marinoan glaciations. A full geological description is provided elsewhere (Kunzmann et al., 2015; Kunzmann et al., 2017b), but, briefly, the succession consists of three groups with ages spanning from ca. 950 Ma to 590 Ma. The basal Veteranen Group records an initial rift-phase of basin development, while the overlying Akademikerbreen and Polarisbreen groups were deposited on a stable, thermally subsiding continental shelf (Halverson et al., 2018). Fe_{HR}/Fe_T ratios primarily imply anoxia with a few samples having values indicative of oxic conditions. RSE concentrations are relatively low

and do not correlate with total organic carbon concentration (Kunzmann et al., 2015). Therefore, these sediments were not deposited under suboxic to anoxic-ferruginous conditions.

3.2.Sample preparation

Shale samples were collected over the course of multiple field seasons and were previously described in detail (Sperling et al., 2015; Gibson et al., 2018; Kunzmann et al., 2017b; Gibson et al., 2020; Hodgskiss et al., 2020). Briefly, fresh samples were selected, cut and cleaned thoroughly to remove weathered surface material before crushing and grinding.

For *aqua regia* leaching, aliquots of 250 to 500 mg rock powder were weighed in Teflon digestion vessels before a mixture of HCl/HNO_3 (double-distilled Trace Metal Grade, 2/6 v/v) was added. The mixture was kept at ca. 120 ºC overnight on a hot plate, after which the supernatant was filtered (0.2 µm, Nylon filter, Sartorius). Around 5 % of the total set of samples were leached in duplicate to assess variability (Supplementary Data S1).

For whole-rock digestion, aliquots of rock powder were mixed with a four-acid mixture (HNO_3/HF/HCl/$HClO_4$, 6/3/2/2, v/v/v/v) and kept at ca. 120 ºC overnight on a hot plate. Clear solutions were dried at 95 ºC before samples were redissolved in 4 mL HCl. The solutions were dried again and a second 4 mL of HCl were added. These steps were designed to dissolve any fluoride precipitate. If needed (brown-colored solutions), 0.5 to 2 mL of H_2O_2 was added in HCl acid media to oxidize any residual organic content. These solutions were dried again before a final 8 mL of 1.5 M HNO_3 solution was added. The vessels were tightly closed and kept at 75 ºC overnight. For each digestion batch, USGS standards BCR-2 and BHVO-2 were also analyzed to verify the analytical procedure.

3.3.Elemental analysis

Elemental concentrations were measured using an 8800 Triple Quadrupole ICP-MS (Agilent Technologies) at the Water Quality Center (Trent University, Canada). Further technical details are provided in Dang et al. (2018b). Briefly, elemental compositions were analyzed in single quadrupole and MS/MS mode with In (20 µg L^{-1}) as an internal standard. Reference materials (ES-L1, EnviroMat) were analyzed every 8-to-10 samples to check recovery and stability. C02A reference standard (CALA, The Canadian Association for Laboratory Accreditation Inc.) was also

used to double check the analytical accuracy. Recovery was determined using solution (analytical recovery, Table S2) and rock certified reference materials (Table S3).

3.4.Uranium isotope analysis

The method for U isotope analysis has been described in Dang et al. (2018b, 2018a, 2016). Briefly, U was purified from sample matrices using TRU resin (100-150 μm, Eichrom). A double spike technique using $^{233}U/^{236}U$ (IRMM-3636b) was used for internal correction of instrumental mass fractionation and any potential isotope fractionation during column purification chemistry. Two double-spiked standards (IRMM-184, prepared in the same matrix as the samples, i.e., 1.5-M HNO_3) were included routinely with each batch of column chemistry (i.e., every 18 samples) to verify the absence of artificial U isotope fractionation during the process (Dang et al., 2018b).

Uranium isotope ratios were measured on a MC-ICP-MS (Thermo Scientific Neptune) at the Trent Water Quality Center. Technical details have been described previously (Dang et al., 2018b; Dang et al., 2018a). Each sample was bracketed by two double-spiked standards (prepared in HCl/HF 0.1M/0.3M solution); the U concentrations were 33 μg L^{-1} in both samples and standards, yielding a signal of ca. 12 V for ^{238}U and 0.1 V for ^{235}U. We also analyzed several procedural blanks; their signals were $(5\pm1)\times10^{-3}$ V for ^{238}U and $(5\pm1)\times10^{-5}$ V for ^{235}U (n=16), which remained a factor of 2,000 lower than the samples and standards. Uranium isotope variation in the sample ($\delta^{238}U$, Eq. 1) was calculated relative to the IRMM-184 standard then converted so that it is reported relative to CRM-145, a more widely used standard for comparison with previously reported data in the literature (see Dang et al., (2018b) for the conversion). The long-term monitoring of U isotope measurement accuracy was performed using the IRMM-184 (double-spiked standard bracket), an in-house reference material (UTS-1, Natural Resources Canada) and USGS standards (BCR-2 and AGV-2). More details are provided in Table S4. External precision of our dataset is usually better than 0.09 ‰ (±2 SD) based on duplicate analyses of reference materials and samples (here and those previously published (Dang et al., 2016; Dang et al., 2018b; Dang et al., 2018a).

4. Results and discussion

4.1.Estimation of the detrital and authigenic U fractions in black shale.

316 Accurate quantification of the detrital and authigenic fractions of RSEs is a prerequisite for paleo-
317 environmental reconstruction (see section 2.2.). In this study, we applied two techniques to assess
318 the U concentration and the U isotope composition of the authigenic and detrital fractions: (i) a
319 selective leaching method using *aqua regia* (Xu et al., 2012) and (ii) an empirical approach based
320 on a fixed detrital U/Al and U/Th ratios (Andersen et al., 2014). For the second technique, we first
321 compared average detrital U/Al ratios for two common bulk elemental reference compositions:
322 upper continental crust (UC), with $U/Al_{UC} = 34.8\times10^{-6}$ (i.e., 34.8 µg g^{-1}, McLennan, 2001) and
323 Post-Archean Australian Shale (PAAS), with $U/Al_{PAAS} = 10.8\times10^{-6}$ (i.e., 10.8 µg g^{-1}, Taylor and
324 McLennan, 1985). The PAAS composite is less enriched in U (e.g., [U] = 0.9 µg g^{-1}, Taylor and
325 McLennan, 1985; Tribovillard et al., 2006) than average Phanerozoic or late Proterozoic shale
326 summarized by the North American Shale Composite (NASC) with [U] = 2.7 µg g^{-1} (Gromet et
327 al., 1984) and the average upper continental crust (UCC), [U] = 2.8 µg g^{-1} (Tribovillard et al.,
328 2006). Application of the higher U/Al_{UC} ratios for the detrital fraction from NASC has resulted in
329 overestimation of the Precambrian detrital U fraction (i.e., exceeding total U concentration for
330 many samples; data not shown). Consequently, we used U/Al_{PAAS} to calculate the authigenic U
331 concentration and isotopic compositions (using a detrital $\delta^{238}U$ of -0.30 ‰, Kendall et al., 2013;
332 Andersen et al., 2017), applying methods and error magnifications as previously reported
333 (Andersen et al., 2014). Similarly, a detrital correction was performed using thorium as the
334 refractory element instead of Al, given the similarities in atomic sizes and elemental behavior of
335 these two actinides (i.e., U and Th); using an average modern detrital U/Th ratio of 0.28 (Cole et
336 al., 2017). Ultimately, because of potentially large uncertainty associated with these empirical
337 calculations for $\delta^{238}U_{authigenic}$, we filtered out all values that showed anomalously high $\delta^{238}U_{authigenic}$
338 (i.e., > +1.2 ‰) and those having uncertainties larger than ±0.5 ‰ (104 samples out of 818). All
339 data are reported in Supplementary Data 2.

340 It is also important to note that the *aqua regia* leaching method can also dissolve the carbonate
341 fraction, which may have high U concentrations and contribute to the bulk U in sediments
342 (Andersen et al., 2017). We estimated the percentage of U in the carbonate fraction assuming a
343 U/Ca ratio of 3.25×10^{-6} and the measured Ca concentrations (Andersen et al., 2014), which

averaged 0.02% (n=51). Therefore, we consider that the carbonate U pool is negligible in the shale samples and thus assigned the leached U to solely the authigenic U fraction.

The calculated U isotope composition in the detrital fraction using the measured $\delta^{238}U$ for the leached as $\delta^{238}U_{authigenic}$ (using Eq. 3) in the Northwestern Canada and Svalbard sample sets (n=24) matches the isotopic signature of the upper crust, with a detrital fraction ($f_{detrital}$) from 40 to 80% (**Fig. S2**). Also, the calculated $\delta^{238}U_{authigenic}$ from fixed U/Al or U/Th detrital ratios displays significantly larger errors than the leaching method, in particular for samples with low authigenic U enrichment (**Fig. 1A**). In samples with larger U enrichment, $\delta^{238}U_{authigenic}$ values determined using the empirical approaches (both U/Al and U/Th) were very similar to those obtained by selective leaching (**Fig. 1, B and C**). These results support the applicability and accuracy of the selective *aqua regia* extraction approach and demonstrate that these leachates yield robust estimates of the isotopic composition of the authigenic U fraction, even in samples with low authigenic U.

4.2.U isotope signatures of shale through time.

Most of the examined shale samples (90 out of 163, bulk and leachates included) have $\delta^{238}U$ values higher than UCC (-0.31±0.14 ‰, **Fig. 2, C and D**). Those values are observed in samples deposited at ca. 1.05, 0.92, 0.82, 0.74, 0.66, 0.65 and 0.63 Ga (**Fig. S3**) and are consistent with previously reported shale-hosted U isotope records of different Precambrian ages (**Fig. 2 C**, e.g., 2.5 Ga (Kendall et al., 2013), 1.98 Ga (Mänd et al., 2020), 1.36 Ga (Yang et al., 2017) and 0.56 Ga (Kendall et al., 2015)). A literature compilation of shale over Earth's History (818 samples including new data from this study, see Supplementary Data S2) shows that the $\delta^{238}U_{authigenic}$ values are generally higher following the GOE compared to the Archaean and earliest Paleoproterozoic, which display muted $\delta^{238}U$ values close to UCC (**Fig. 2 C and D**). These changes in the U isotope composition over time are not evident from the bulk $\delta^{238}U$ measurements alone (**Fig. 2C**). For example, most of the Neoproterozoic samples show $\delta^{238}U_{bulk}$ signatures close to UCC (green circles in **Fig. 2C**) due to their relatively large detrital U fraction (>40%; e.g., **Fig. S2B**).

The observed high $\delta^{238}U_{authigenic}$ (up to 0.9 ‰, **Fig. 2D**) compositions following the late Proterozoic are interpreted to record deposition within a partially oxygenated ocean for two reasons. First, large U isotope fractionations are mainly associated with partial reduction of U^{VI} to U^{IV} (Wang et

al., 2020), while under more extreme anoxic conditions, near-quantitative U removal yields no net isotope fractionation, i.e., muted fractionation (Andersen et al., 2014). Second, relatively high $\delta^{238}U_{authigenic}$ compositions are more likely associated with a smaller U reservoir resulting from limited connectivity to the open ocean (Lau et al., 2020). This phenomenon is observed today in the Black Sea and Lake Rogoznica (Andersen et al., 2017; Rolison et al., 2017; Bura-Nakić et al., 2018; Lau et al., 2020).

To further evaluate the temporal shifts of $\delta^{238}U$ in the shale record, both the bulk and authigenic $\delta^{238}U$ fractions were time-binned in frequency histograms (**Fig. S4**). Five bin ranges were selected: (i) Pre-GOE (>2.46 Ga, Gumsley et al., (2017)), (ii) Early-Middle Proterozoic (2.46-1.1 Ga), (iii) Late Proterozoic (1.1-0.55 Ga), (iv) Phanerozoic pre-Holocene and (v) Holocene (**Table 1**). Although it is recognized that large fluctuations in atmospheric oxygen levels likely occurred during the Paleoproterozoic Era, available data are insufficient to subdivide the early and middle Proterozoic. Also, the Holocene bin was separated from the Phanerozoic because those samples constitute a dataset (n = 352) acquired from well-characterized, modern depositional environments that include oxic, suboxic and euxinic basins.

To test whether there is a significant distinction in $\delta^{238}U$ values between the temporal bins, we generated bootstrap resampled mean values for $\delta^{238}U$ (**Table 1**) for both the authigenic (**Fig. 3**) and bulk fractions (**Fig. S5**). The $\delta^{238}U_{authigenic}$ values were calculated using the empirical approach and published data when Al concentrations were available, whereas both the *aqua regia*-leached data (n=134) and empirical approaches (n= 28) were used for samples in this study.

Table 1: Bootstrap resampled mean of bulk and authigenic $\delta^{238}U$ over the geologic time intervals.

Temporal bins	Age	Bulk $\delta^{238}U$ (n)	Authigenic $\delta^{238}U$ (n)
Pre-GOE	3.5 to 2.46 Ga	-0.27±0.01 ‰ (190)	-0.27±0.01 ‰ (151)
Post-GOE	2.46 to 1.1 Ga	-0.04±0.03 ‰ (98)	-0.06±0.03 ‰ (80)
Late Proterozoic	1.1 to 0.55 Ga	+0.04±0.04 ‰ (75)	-0.02±0.02 ‰ (202*)
Phanerozoic (pre-Holocene)	0.55 to 0.01 Ga	+0.11±0.02 ‰ (100)	+0.12±0.02 ‰ (96)
Holocene	0.01 Ga to present	-0.06±0.01 ‰ (352)	-0.05±0.01 ‰ (325)

* includes (i) the empirically-calculated data from the literature (n=40), (ii) the empirically-calculated data from this study (n=28), and (iii) results of the *aqua regia* leach (n=134).

The mean $\delta^{238}U_{authigenic}$ value for pre-GOE samples is -0.27±0.01 ‰ (**Fig. 3**), similar to that of the upper continental crust (-0.31±0.14 ‰, Kendall et al., 2013). This convergence is presumably the result of limited oxidative weathering, a small oceanic U reservoir, and a largely anoxic ocean characterized by near-quantitative U removal. All other bins show progressively more positive $\delta^{238}U$ values, suggesting enhanced oxidative weathering of U^{IV}-bearing minerals, a larger U^{IV} oceanic reservoir and U isotope fractionation during removal into the sediment compared to the pre-GOE period (Wang et al., 2018). Indeed, the $\delta^{238}U_{authigenic}$ bootstrapped mean for Early-Middle Proterozoic data increases to -0.06±0.03 ‰ (**Table 1**). This trend towards higher $\delta^{238}U_{authigenic}$ mean values continues into the late Proterozoic and Phanerozoic pre-Holocene bins (-0.2±0.03 ‰ and +0.12±0.03 ‰, respectively), consistent with broadly increasing oxygen abundances through time (Wang et al., 2018). Paradoxically, the $\delta^{238}U$ mean value for the Holocene ($\delta^{238}U_{authigenic}$ = -0.05±0.01 ‰) is lower than the Phanerozoic pre-Holocene and Neoproterozoic. One potential explanation for the difference may be that it is an artifact of sampling bias between the modern and ancient shale samples. Specifically, the modern shale record is dominated by samples from semi-restricted anoxic basins (e.g., Cariaco Basin, Black Sea). Here, the rate of U drawdown outcompetes the U influx into the basin, resulting in significantly lower local U residence times and muted $\Delta^{238}U$ relative to the open-ocean $\delta^{238}U$ composition. Also, the diversity in depositional environments (e.g., oxic, hypoxic, anoxic/euxinic, Andersen et al., 2017) for the modern samples is likely not matched by the Phanerozoic pre-Holocene and Neoproterozoic samples, which were collected dominantly from shale deposited in ferruginous environments (Guilbaud et al., 2015). Clearly, the isotope fractionation of U uptake into shale depends on the specific local environment and may be large in certain circumstances. Also, the oceanic residence time of U likely changed drastically over Earth's history as a result of changes in magnitude of oxidative sources and reductive sinks (Chen et al., 2021). Therefore, the high $\delta^{238}U$ observed in the Neoproterozoic shale and Phanerozoic pre-Holocene samples (**Fig. 3**) may be related to a specific environmental setting that favored large U isotope fractionation.

In summary, our late Proterozoic $\delta^{238}U$ data show a clear transition in the U isotope systematics toward the Phanerozoic pre-Holocene (**Fig. 3**). The increased $\delta^{238}U_{authigenic}$ from 1.05 to 0.63 Ga of this dataset (**Fig. 2D**) and the time-binned evolution of the shale-hosted U isotopes over time (**Fig. 3**), in conjunction with other previously published paleo-redox proxy data (e.g., carbonate Cr isotopes, RSEs, biomarkers, see section 1) suggest several transient periods of ocean oxygenation during this interval of the late Proterozoic. Yet, the interpretation of oceanic oxygenation events based on authigenic U isotope compositions in organic-rich shale requires full consideration of the reservoir it tracks (i.e., local rather than a global reservoir), as well as how specific biogeochemical marine environments impact U isotope systematics at the basin scale.

4.3.U isotope systematics and late Proterozoic oxygenation history at the basin scale.

To understand how specific redox states influence the U isotope composition of shale, it is first necessary to determine the local redox conditions in the samples and at the basin scale. Iron speciation chemistry is a well-established paleo-redox proxy that tracks the local redox state of the water column (Sperling et al., 2015; Raiswell et al., 2018). This proxy distinguishes the water column chemistry as being either oxic (with dissolved O_2), ferruginous (anoxic with free ferrous iron) or euxinic (anoxic with dissolved hydrogen sulfide) (Poulton and Canfeld, 2011; Cole et al., 2020a).

Iron speciation data for samples from northwestern Canada and Greenland indicate low abundances of highly reactive iron (Fe_{HR}) and pyrite (Fe_{Py}) (**Fig. 4, A and B**; Kunzmann et al., 2017b; Gibson et al., 2020) in samples that show significant U isotope fractionation ($\delta^{238}U_{authigenic}$ up to +1 ‰, **Fig. 4, C and D**). In addition, these samples also record very low authigenic U (<2 ppm) and Mo (< 5 ppm) with Mo/U ratios well below 1 relative to the modern seawater composition (**Fig. 4, E and F**). These Mo/U ratios also eliminate the possibility of euxinic conditions, which would favor the authigenic Mo fluxes to the sediment over U (Algeo and Tribovillard, 2009). Collectively, these data imply dominantly suboxic (trace amounts of dissolved O_2) to oxic conditions (20 out of 26 samples) rather than ferruginous conditions (six out of 26 samples). Under these conditions, U is not quantitatively removed from seawater, allowing large U isotope fractionation to be expressed (Andersen et al., 2014; Lau et al., 2020).

In contrast, Fe speciation data for samples from Baffin Island (Hodgskiss et al., 2020) and Svalbard (Kunzmann et al., 2017) indicate dominantly ferruginous conditions with only a few samples (7 out of 63) suggesting oxic conditions (**Fig. 5, A and B**). These samples record higher authigenic U (up to 5 ppm) and Mo (up to 35 ppm) enrichments with Mo/U ratios up to three times higher than the modern seawater Mo/U ratios (**Fig. 5, E and F).** This situation could be interpreted either as sulfidic conditions or the existence of particulate shuttle linked to Mn-Fe redox cycling within the water column (Algeo and Tribovillard, 2009). Given the Fe speciation data (**Fig. 5, A and B**), the latter hypothesis is more likely correct. Correspondingly, $\delta^{238}U$ in these samples is lower (i.e., $\delta^{238}U$ up to 0.5 ‰, **Fig. 5, C and D**) compared to samples from Northwestern Canada and Greenland.

Ferruginous conditions are considered to have been widespread through the majority of Earth's history (Planavsky et al., 2011; Sperling et al., 2015). It is therefore crucial to assess the extent of U isotope fractionation under such specific conditions. Cole et al. (2020b) assessed U isotope fractionation in sediment from two modern stratified lakes with permanent anoxic bottom waters, the Peru Margin Oxygen Minimum Zone, and Silurian-Devonian shale to constrain U isotope fractionation in anoxic and iron-rich aquatic systems. The authors reported highly variable U isotope fractionations in these environments ($\delta^{238}U_{authigenic}$ from -0.8‰ to +0.64 ‰), which overlap and become indistinguishable from oxic settings.

First, the calculated $\delta^{238}U_{authigenic}$ values from Cole et al. (2020b) have significantly large uncertainties associated with the empirical calculations. Variations in the $\delta^{238}U_{bulk}$ are indeed narrower for the two modern anoxic lakes (-0.32 to +0.36 ‰ and -0.53 to +0.01‰, respectively). These ranges corresponded to a maximum U isotope fractionation ($\Delta_{bulk}^{anoxic/ferruginous}$) of ~0.6 ‰, which is similar to the range observed in the samples from Baffin Island and Svalbard (**Fig. 5**). Second, Cole et al. (2020b) also reported very low $\delta^{238}U_{authigenic}$ values (i.e., -0.81 to -0.4 ‰) from the modern sediments of Lake Pavin and Brownie Lake, below the $\delta^{238}U_{crust}$ (-0.31±0.14 ‰; Kendall et al., 2013). Such low $\delta^{238}U$ data were also reported in anoxic sediments and are likely to be related to U sorption onto ferromanganese oxides or U deposition with organic matter (Hinojosa et al., 2016; Abshire et al., 2020; Andersen et al., 2020). The former is accompanied by a -0.2 ‰ fractionation (Brennecka et al., 2011; Dang et al., 2016) while the latter was demonstrated both in

lab experiments and natural samples (plankton tow and sediment traps) to have $\delta^{238}U$ between -0.5 and -1.24 ‰ (Holmden et al., 2015; Chen et al., 2020). Another study investigated both bulk and porewater $\delta^{238}U$ in two different lakes: Bentley Lake, a meromictic lake with permanent anoxic bottom water and Bow Lake, which experiences annual turn-overs (Wang et al., 2019). This study reported a positive U isotope fractionation in subsurface sediment of Bow Lake but negative $\Delta^{238}U$ in Bentley Lake. This likely indicates distinct biogeochemical reactions in the top sediment layer of anoxic and oxic modern lakes. Third, modern anoxic aquatic systems record significant spatial heterogeneity. In Bow Lake, U isotope fractionation ranges from 0.1 to 0.5 ‰ in sediments below the thermocline across the lake, and the extent of $\Delta^{238}U$ is controlled by bacterial diversity (*Geobacteraceae* and sulphate-reducing bacteria) and the quality of bioavailable organic matter (Dang et al., 2018b). In summary, there are various environmental factors (e.g., presence of ferromanganese oxides at the sediment-water inferace, deposition of U bound to fresh organic matter and sedimentary bacterial activities) and methodological approaches (e.g., to extract the authigenic U isotope signature) that could lead to the large variability of $\Delta^{238}U_{anoxic}$ in modern depositional settings as reported by Cole et al. (2020b). Also, it is important to note the challenges associated with the extrapolation of understanding from modern anoxic aquatic systems into ancient oceans, as extensively discussed by Chen et al. (2021). However, our data suggest that the extent of U isotope fractionation under anoxic (ferruginous) conditions, in both modern (Dang et al., 2018b) and ancient samples (Baffin Island and Svalbard), would be between 0.1 and 0.6 ‰, although more studies are required to refine this range.

4.4. Implication for integrating the late Proterozoic geochemical record and biological evolution

The occurrence of dominantly ferruginous and oxic conditions in all the examined shale of this study is consistent with limited marine euxinia between 1.05 to 0.66 Ga (Sperling et al., 2015; Gilleaudeau et al., 2019), and also with independent evidence for a broad transition from more euxinic to more ferruginous deep-water conditions in the early Neoproterozoic (Guilbaud et al., 2015). Iron isotope data on late Tonian shale also indicates dominantly ferruginous conditions prior to the onset of Cryogenian glaciations (Kunzmann et al., 2017b), and widespread occurrence of iron formation in Sturtian (0.717 to 0.66 Ga) glacial successions indicate that iron-rich deep waters persisted into at least the early Cryogenian Period (Cox et al., 2013). A significant shift in

510 the iron isotope composition of shale following the Sturtian glaciation suggests the partial
511 oxidation of the ferrous seawater reservoir although other data sets, including U isotope signatures
512 in carbonate, have been used to argue for at least transient oxygenation at this time (Lau et al.,
513 2017).

514 Thus, local paleo-redox proxies suggest that late Proterozoic oceans were largely ferruginous with
515 limited euxinic environments that were most likely confined to productive continental margins
516 (Guilbaud et al., 2015). Ferruginous conditions may be important for oceanic U cycling because
517 of the high abundance of highly reactive ferrous ions, such as iron (II/III) (oxyhyr)oxide mineral
518 phases (Kunzmann et al., 2017b). In fact, U^{VI}, if present, may interact with mixed valence iron
519 phases (e.g., magnetite and green rust) such that increased Fe^{II}/Fe^{III} ratios result in more U being
520 precipitated as U^{IV} (Roberts et al., 2017). However, the impact of ferruginous conditions (i.e., with
521 abundant reactive ferrous iron species) on U isotope systematics must be considered in the context
522 of mass balance and the specific fractionation factors for U removal by this pathway. For instance,
523 it is inferred that the U isotope fractionation factor for water column U(IV) removal may be
524 significantly larger than from U reduction from pore-waters within sediment, where this reaction
525 is more likely to be limited by availability of electron donors and diffusion (Andersen et al., 2014;
526 Dang et al., 2018a). However, if U removal is largely quantitative, the expressed U isotope
527 fractionation would be muted. Thus, a better quantification of the U sink in a ferruginous ocean
528 would help constrain ocean oxygenation levels.

529 In this light, it was previously suggested that the Ediacaran ocean was characterized by anoxia but
530 marked by episodic transient oxygenation events (Sahoo et al., 2016). Our data suggests that such
531 events may have commenced earlier in the Neoproterozoic or even the Mesoproterozoic Era. In
532 other words, late Proterozoic oceans were unlikely characterized by monotonous anoxic
533 conditions, but may have been rather redox dynamic, and sensitive to relatively small changes in
534 oxygen sinks or sources (Cole et al., 2020a). Wood and Erwin (2018) suggested that dynamic-
535 redox environments favored morphological novelty, which can promote subsequent radiation and
536 diversification. In the late Proterozoic, the protracted oceanic oxygenation recorded in U isotope
537 systematics in this study and data compiled from the literature correspond to (i) the appearance of
538 eukaryotic photosynthetic crown-groups (**Fig. 2B**) and (ii) eukaryotic diversification with major

evolutionary innovations (e.g., eukaryovory, biomineralization, cyanobacterial heterocysts (0.82 to 0.54 Ga) (Xiao and Tang, 2018). Therefore, the U isotope record provides support for favorable environmental conditions for adaptation and diversification of early eukaryotic clades in the late Mesoproterozoic to Neoproterozoic eras.

5. Conclusion.

Shale samples are composed of both detrital and authigenic fractions of the elements and their isotopes. We assessed and compared the applicability of an *aqua regia* leaching process on ancient samples, where authigenic U concentrations are low and thus overwhelmed by detrital U, to the empirical calculation based on fixed U/Al or U/Th ratios. The former seems to be robust and carries less uncertainty than the empirical approach. In cases where the authigenic U fraction is overwhelmed by the detrital U fraction in ancient samples (Wang et al., 2020), the leaching approach could provide valuable information on the application of RSEs and their isotopes as paleo-redox proxies.

Our shale-hosted $\delta^{238}U_{authigenic}$ record provides a wide-ranging archive of changes in the oxygenation history across several late Proterozoic sedimentary records. The U isotope data presented herein, in conjunction with existing Fe speciation data, provide a nuanced perspective of the redox conditions from four late Proterozoic sedimentary basins. Samples from Baffin Island and Svalbard were deposited in environments that were dominantly ferruginous, with muted RSE enrichment and $\delta^{238}U_{authigenic}$ compositions indicating moderate U isotope fractionation ($\Delta^{238}U$ up to +0.6 ‰). However, samples from Greenland and NW Canada reflect deposition in more oxic conditions where RSEs were not highly enriched but $\delta^{238}U_{authigenic}$ compositions suggest U isotope fractionation was more pronounced ($\Delta^{238}U$ up to 1.2 ‰).

Finally, the earliest increase of U isotope compositions of our dataset at ca. 1.05 Ga roughly corresponds with estimates for the origin of eukaryotic photosynthesis (Gibson et al., 2018). Together with other paleo-redox proxies (Fe speciation and isotopes), these data suggest changes in the basin's redox status with possible transient oxygenation, at least locally, superimposed on a background of ferruginous conditions in the late Proterozoic deep ocean. The degree of oxygenation may have not been sufficient to drastically change the ocean redox state as much as

in the early Phanerozoic but may have been sufficient to promote oxidative cycling of Fe, U and other RSEs.

Acknowledgments: R.D.E, W.W., D.H.D., and G.P.H. acknowledge funding from the Natural Sciences and Engineering Research Council of Canada (NSERC), the Agouron Institute, and Natural Resources Canada. T.M.G. acknowledges an Agouron Geobiology Fellowship. M.B.A. acknowledges NERC NE/V004824/1. The authors thank Dr. Bastian Georg, Kelsey Lamothe and Dr. Hayla Evans for assistance with isotope measurements, Fe speciation analysis and manuscript preparation, respectively.

Competing interests: Authors declare no competing interests.

Data and materials availability: All data is available in the main text or the supplementary materials.

578 **References:**

579 Abshire M. L., Romaniello S. J., Kuzminov A. M., Cofrancesco J., Severmann S. and Riedinger
580 N. (2020) Uranium isotopes as a proxy for primary depositional redox conditions in
581 organic-rich marine systems. *Earth Planet. Sci. Lett.* **529**, 115878. Available at:
582 https://doi.org/10.1016/j.epsl.2019.115878.

583 Van Acken D., Thomson D., Rainbird R. H. and Creaser R. A. (2013) Constraining the
584 depositional history of the Neoproterozoic Shaler Supergroup, Amundsen Basin, NW
585 Canada: Rhenium-osmium dating of black shales from the Wynniatt and Boot Inlet
586 Formations. *Precambrian Res.* **236**, 124–131.

587 Algeo T. J. and Tribovillard N. (2009) Environmental analysis of paleoceanographic systems
588 based on molybdenum – uranium covariation. *Chem. Geol.* **268**, 211–225.

589 Andersen M. B., Matthews A., Bar-Matthews M. and Vance D. (2020) Rapid onset of ocean
590 anoxia shown by high U and low Mo isotope compositions of sapropel S1. *Geochemical*
591 *Perspect. Lett.* **15**, 10–14.

592 Andersen M. B., Romaniello S., Vance D., Little S. H., Herdman R. and Lyons T. W. (2014) A
593 modern framework for the interpretation of 238U/235U in studies of ancient ocean redox.
594 *Earth Planet. Sci. Lett.* **400**, 184–194. Available at:
595 http://dx.doi.org/10.1016/j.epsl.2014.05.051.

596 Andersen M. B., Stirling C. H. and Weyer S. (2017) Uranium Isotope Fractionation. In *Reviews*
597 *in Mineralogy & Geochemistry* (eds. F.-Z. Teng, J. Watkins, and N. Dauphas). pp. 799–850.

598 Andersen M. B., Vance D., Morford J. L., Bura-Nakić E., Breitenbach S. F. M. and Och L.
599 (2016) Closing in on the marine 238U/235U budget. *Chem. Geol.* **420**, 11–22.

600 Barnes C. E. and Cochran J. K. (1990) Uranium removal in oceanic sediments and the oceanic U
601 balance. *Earth Planet. Sci. Lett.* **97**, 94–101.

602 Brennecka G., Wasylenki L. E., Weyer S. and Anbar a D. (2011) Uranium isotope fractionation
603 during adsorption to manganese oxides. *Environ. Sciene Technol.* **45**, 1370–1375.

604 Bura-Nakić E., Andersen M. B., Archer C., de Souza G. F., Marguš M. and Vance D. (2018)
605 Coupled Mo-U abundances and isotopes in a small marine euxinic basin: Constraints on
606 processes in euxinic basins. *Geochim. Cosmochim. Acta* **222**, 212–229.

607 Butterfield N. J. (2000) Bangiomorpha pubescens n. gen., n. sp.: implications for the evolution of
608 sex, multicellularity, and the Mesoproterozoic/Neoproterozoic radiation of eukaryotes.
609 *Paleobiology* **26**, 386–404.

610 Butterfield N. J. (2009) Oxygen, animals and oceanic ventilation: An alternative view.
611 *Geobiology* **7**, 1–7.

612 Canfield D. E., Zhang S., Frank A. B., Wang X., Wang H., Su J., Ye Y. and Frei R. (2018)
613 Highly fractionated chromium isotopes in Mesoproterozoic-aged shales and atmospheric
614 oxygen. *Nat. Commun.* **9**, 1–11.

615 Chen X., Tissot F. L. H., Jansen M. F., Bekker A., Liu C. X., Nie N. X., Halverson G. P., Veizer

J. and Dauphas N. (2021) The Uranium Isotopic Record of Shales and Carbonates Through Geologic Time. *Geochim. Cosmochim. Acta*, In Press.

Chen X., Zheng W. and Anbar A. D. (2020) Uranium Isotope Fractionation (238U/235U) during U(VI) Uptake by Freshwater Plankton. *Environ. Sci. Technol.* **54**, 2744–2752.

Cheng M., Li C., Chen X., Zhou L., Algeo T. J., Ling H. F., Feng L. J. and Jin C. S. (2018) Delayed Neoproterozoic oceanic oxygenation: Evidence from Mo isotopes of the Cryogenian Datangpo Formation. *Precambrian Res.* **319**, 187–197.

Cole D. B., Mills D. B., Erwin D. H., Sperling E. A., Porter S. M., Reinhard C. T. and Planavsky N. J. (2020a) On the co-evolution of surface oxygen levels and animals. *Geobiology* **18**, 260–281.

Cole D. B., Planavsky N. J., Longley M., Böning P., Wilkes D., Wang X., Swanner E. D., Wittkop C., Loydell D. K., Busigny V., Knudsen A. C. and Sperling E. A. (2020b) Uranium Isotope Fractionation in Non-sulfidic Anoxic Settings and the Global Uranium Isotope Mass Balance. *Global Biogeochem. Cycles* **34**, e2020GB006649.

Cole D. B., Reinhard C. T., Wang X., Gueguen B., Halverson G. P., Gibson T., Hodgskiss M. S. W., Ryan McKenzie N., Lyons T. W. and Planavsky N. J. (2016) A shale-hosted Cr isotope record of low atmospheric oxygen during the Proterozoic. *Geology* **44**, 555–558.

Cole D. B., Zhang S. and Planavsky N. J. (2017) A new estimate of detrital redox-sensitive metal concentrations and variability in fluxes to marine sediments. *Geochim. Cosmochim. Acta* **215**, 337–353.

Cox G. M., Halverson G. P., Minarik W. G., Le Heron D. P., Macdonald F. A., Bellefroid E. J. and Strauss J. V. (2013) Neoproterozoic iron formation: An evaluation of its temporal, environmental and tectonic significance. *Chem. Geol.* **362**, 232–249.

Crockford P. W., Hayles J. A., Bao H., Planavsky N. J., Bekker A., Fralick P. W., Halverson G. P., Bui T. H., Peng Y. and Wing B. A. (2018) Triple oxygen isotope evidence for limited mid-Proterozoic primary productivity. *Nature* **559**, 613–616.

Dahl T. W., Hammarlund E. U., Anbar A. D., Bond D. P. G., Gill B. C., Gordon G. W., Knoll A. H., Nielsen A. T., Schovsbo N. H. and Canfield D. E. (2010) Devonian rise in atmospheric oxygen correlated to the radiations of terrestrial plants and large predatory fish. *Proc. Natl. Acad. Sci. U. S. A.* **107**, 17911–17915.

Dang D. H., Evans R. D., Wang W., Omanović D., Houssainy A. El, Lenoble V., Mullot J., Mounier S. and Garnier C. (2018a) Uranium isotope geochemistry in modern coastal sediments: Insights from Toulon Bay, France. *Chem. Geol.* **481**, 133–145.

Dang D. H., Novotnik B., Wang W., Georg R. B. and Evans D. (2016) Uranium isotope fractionation during adsorption, (co)precipitation and biotic reduction. *Environ. Sci. Technol.* **50**, 12695–12704.

Dang D. H., Wang W., Pelletier P., Poulain A. J. and Evans D. (2018b) Uranium dispersion from U tailings and mechanisms leading to U accumulation in sediments: insights from biogeochemical and isotopic approaches. *Sci. Total Environ.* **610–611**, 880–891.

Dunk R. M., Mills R. A. and Jenkins W. J. (2002) A reevaluation of the oceanic uranium budget for the Holocene. *Chem. Geol.* **190**, 45–67.

Erwin D. H., Laflamme M., Tweedt S. M., Sperling E. A., Pisani D. and Peterson K. J. (2011) The Cambrian conundrum: Early divergence and later ecological success in the early history of animals. *Science (80-.).* **334**, 1091–1097.

Gibson T. M., Kunzmann M., Poirier A., Schumann D., Tosca N. J. and Halverson G. P. (2020) Geochemical signatures of transgressive shale intervals from the 811 Ma Fifteenmile Group in Yukon, Canada: Disentangling sedimentary redox cycling from weathering alteration. *Geochim. Cosmochim. Acta* **280**, 161–184.

Gibson T. M., Shih P. M., Cumming V. M., Fischer W. W., Crockford P. W., Hodgskiss M. S. W., Wörndle S., Creaser R. A., Rainbird R. H., Skulski T. M. and Halverson G. P. (2018) Precise age of Bangiomorpha pubescens dates the origin of eukaryotic photosynthesis. *Geology* **46**, 135–138.

Gibson T. M., Wörndle S., Crockford P. W., Hao Bui T., Creaser R. A. and Halverson G. P. (2019) Radiogenic isotope chemostratigraphy reveals marine and nonmarine depositional environments in the late Mesoproterozoic Borden Basin, Arctic Canada. *Bull. Geol. Soc. Am.* **131**, 1965–1978.

Gilleaudeau G. J., Frei R., Kaufman A. J., Kah L. C., Azmy K., Bartley J. K., Chernyavskiy P. and Knoll A. H. (2016) Oxygenation of the mid-Proterozoic atmosphere: Clues from chromium isotopes in carbonates. *Geochemical Perspect. Lett.* **2**, 178–187.

Gilleaudeau G. J., Romaniello S. J., Luo G., Kaufman A. J., Zhang F., Klaebe R. M., Kah L. C., Azmy K., Bartley J. K., Zheng W., Knoll A. H. and Anbar A. D. (2019) Uranium isotope evidence for limited euxinia in mid-Proterozoic oceans. *Earth Planet. Sci. Lett.* **521**, 150–157.

Goto K. T., Sekine Y., Ito T., Suzuki K., Anbar A. D., Gordon G. W., Harigane Y., Maruoka T., Shimoda G., Kashiwabara T., Takaya Y., Nozaki T., Hein J. R., Tetteh G. M., Nyame F. K. and Kiyokawa S. (2021) Progressive ocean oxygenation at ~ 2 . 2 Ga inferred from geochemistry and molybdenum isotopes of the Nsuta Mn deposit , Ghana. *Chem. Geol.* **567**, 120116.

Gromet L. P., Haskin L. A., Korotev R. L. and Dymek R. F. (1984) The "North American shale composite": Its compilation, major and trace element characteristics. *Geochim. Cosmochim. Acta* **48**, 2469–2482.

Guilbaud R., Poulton S. W., Butterfield N. J., Zhu M. and Shields-Zhou G. A. (2015) A global transition to ferruginous conditions in the early Neoproterozoic oceans. *Nat. Geosci.* **8**, 1–5.

Gumsley A. P., Chamberlain K. R., Bleeker W., Söderlund U., de Kock M. O., Larsson E. R. and Bekker A. (2017) Timing and tempo of the Great Oxidation Event. *Proc. Natl. Acad. Sci.* **114**, 1811–1816.

Halverson G. P., Kunzmann M., Strauss J. V and Maloof A. C. (2018) The Tonian-Cryogenian transition in Northeastern Svalbard. *Precambrian Res.* **319**, 79–95.

694 Henderson G. M. and Anderson R. F. (2003) The U-series toolbox for paleoceanography. *Rev.*
695 *Mineral. Geochemistry* **52**, 493–531.

696 Hinojosa J. L., Stirling C. H., Reid M. R., Moy C. M. and Wilson G. S. (2016) Trace metal
697 cycling and 238U/235U in New Zealand's fjords: Implications for reconstructing global
698 paleoredox conditions in organic-rich sediments. *Geochim. Cosmochim. Acta* **179**, 89–109.

699 Hodgskiss M. S. W., Crockford P. W., Peng Y., Wing B. A. and Horner T. J. (2019) A
700 productivity collapse to end Earth's Great Oxidation. *Proc. Natl. Acad. Sci. U. S. A.* **116**,
701 17207–17212.

702 Hodgskiss M. S. W., Sansjofre P., Kunzmann M., Sperling E. A., Cole D. B., Crockford P. W.,
703 Gibson T. M. and Halverson G. P. (2020) A high-TOC shale in a low productivity world:
704 the late Mesoproterozoic Arctic Bay Formation, Nunavut. *Earth Planet. Sci. Lett.* **544**,
705 116384.

706 Holmden C., Amini M. and Francois R. (2015) Uranium isotope fractionation in Saanich Inlet: A
707 modern analog study of a paleoredox tracer. *Geochim. Cosmochim. Acta* **153**, 202–215.

708 Jaffey A. H., Flynn K. F., Glendenin L. E., Bentley W. C. and Essling A. M. (1971) Precision
709 Measurement of Half-Lives and Specific Activities of 235U and 238U. *Phys. Rev. C* **4**,
710 1889–1906.

711 Kendall B., Brennecka G. A., Weyer S. and Anbar A. D. (2013) Uranium isotope fractionation
712 suggests oxidative uranium mobilization at 2.50Ga. *Chem. Geol.* **362**, 105–114.

713 Kendall B., Komiya T., Lyons T. W., Bates S. M., Gordon G. W., Romaniello S. J., Jiang G.,
714 Creaser R. A., Xiao S., McFadden K., Sawaki Y., Tahata M., Shu D., Han J., Li Y., Chu X.
715 and Anbar A. D. (2015) Uranium and molybdenum isotope evidence for an episode of
716 widespread ocean oxygenation during the late ediacaran period. *Geochim. Cosmochim. Acta*
717 **156**, 173–193.

718 Knoll A. H. (2014) Paleobiological perspectives on early eukaryotic evolution. *Cold Spring*
719 *Harb. Perspect. Biol.* **6**, a016121.

720 Krause A. J., Mills B. J. W., Zhang S., Planavsky N. J., Lenton T. M. and Poulton S. W. (2018)
721 Stepwise oxygenation of the Paleozoic atmosphere. *Nat. Commun.* **9**, 1–10.

722 Kunzmann M., Bui T. H., Crockford P. W., Halverson G. P., Scott C., Lyons T. W. and Wing B.
723 A. (2017a) Bacterial sulfur disproportionation constrains timing of neoproterozoic
724 oxygenation. *Geology* **45**, 207–210.

725 Kunzmann M., Gibson T. M., Halverson G. P., Hodgskiss M. S. W., Bui T. H., Carozza D. A.,
726 Sperling E. A., Poirier A., Cox G. M. and Wing B. A. (2017b) Iron isotope biogeochemistry
727 of Neoproterozoic marine shales. *Geochim. Cosmochim. Acta* **209**, 85–105.

728 Kunzmann M., Halverson G. P., Scott C., Minarik W. G. and Wing B. A. (2015) Geochemistry
729 of Neoproterozoic black shales from Svalbard: Implications for oceanic redox conditions
730 spanning Cryogenian glaciations. *Chem. Geol.* **417**, 383–393.

731 Lau K. V., Lyons T. W. and Maher K. (2020) Uranium reduction and isotopic fractionation in
732 reducing sediments: Insights from reactive transport modeling. *Geochim. Cosmochim. Acta*

733 **287**, 65–92.

734 Lau K. V., Macdonald F. A., Maher K. and Payne J. L. (2017) Uranium isotope evidence for
735 temporary ocean oxygenation in the aftermath of the Sturtian Snowball Earth. *Earth Planet.*
736 *Sci. Lett.* **458**, 282–292.

737 Lenton T. M., Boyle R. A., Poulton S. W., Shields-Zhou G. A. and Butterfield N. J. (2014) Co-
738 evolution of eukaryotes and ocean oxygenation in the Neoproterozoic era. *Nat. Geosci.* **7**,
739 257–265.

740 Liu A., Tang D., Shi X., Zhou X., Zhou L., Shang M., Li Y. and Fang H. (2020)
741 Mesoproterozoic oxygenated deep seawater recorded by early diagenetic carbonate
742 concretions from the Member IV of the Xiamaling Formation, North China. *Precambrian*
743 *Res.* **341**, 105667.

744 Lyons T. W., Anbar A. D., Severmann S., Scott C. and Gill B. C. (2009) Tracking Euxinia in the
745 Ancient Ocean: A Multiproxy Perspective and Proterozoic Case Study. *Annu. Rev. Earth*
746 *Planet. Sci.* **37**, 507–534.

747 Lyons T. W., Reinhard C. T. and Planavsky N. J. (2014) The rise of oxygen in Earth's early
748 ocean and atmosphere. *Nature* **506**, 307–15.

749 Mänd K., Lalonde S. V, Robbins L. J., Thoby M., Paiste K., Kreitsmann T., Paiste P., Reinhard
750 C. T., Romashkin A. E., Planavsky N. J., Kirsimäe K., Lepland A. and Konhauser K. O.
751 (2020) Palaeoproterozoic oxygenated oceans following the Lomagundi-Jatuli Event. *Nat.*
752 *Geosci.* **13**, 302–306.

753 McLennan S. M. (2001) Relationships between the trace element composition of sedimentary
754 rocks and upper continental crust. *Geochemistry, Geophys. Geosystems* **2**, 2000GC000109.

755 Mills D. B., Ward L. M., Jones C., Sweeten B., Forth M., Treusch A. H. and Canfield D. E.
756 (2014) Oxygen requirements of the earliest animals. *Proc. Natl. Acad. Sci.* **111**, 4168–4172.

757 Narbonne G. M. (2004) Modular construction of early Ediacaran complex life forms. *Science*
758 *(80-.).* **305**, 1141–1144.

759 Partin C. A., Bekker A., Planavsky N. J., Scott C. T., Gill B. C., Li C., Podkovyrov V., Maslov
760 A., Konhauser K. O., Lalonde S. V., Love G. D., Poulton S. W. and Lyons T. W. (2013)
761 Large-scale fluctuations in Precambrian atmospheric and oceanic oxygen levels from the
762 record of U in shales. *Earth Planet. Sci. Lett.* **369**–**370**, 284–293.

763 Planavsky N. J., McGoldrick P., Scott C. T., Li C., Reinhard C. T., Kelly A. E., Chu X., Bekker
764 A., Love G. D. and Lyons T. W. (2011) Widespread iron-rich conditions in the mid-
765 Proterozoic ocean. *Nature* **477**, 448–451.

766 Planavsky N. J., Reinhard C. T., Wang X., Thomson D., McGoldrick P., Rainbird R. H., Johnson
767 T., Fischer W. W. and Lyons T. W. (2014) Low mid-proterozoic atmospheric oxygen levels
768 and the delayed rise of animals. *Science (80-.).* **346**, 635–638.

769 Poulton S. W. and Canfeld D. E. (2011) Ferruginous conditions: A dominant feature of the ocean
770 through Earth's history. *Elements* **7**, 107–112.

771 Raiswell R., Hardisty D. S., Lyons T. W., Canfield D. E., Owens J. D., Planavsky N. J., Poulton
772 S. W. and Reinhard C. T. (2018) The iron paleoredox proxies: A guide to the pitfalls,
773 problems and proper practice. *Am. J. Sci.* **318**, 491–562.

774 Roberts H. E., Morris K., Law G. T. W., Mosselmans J. F. W., Bots P., Kvashnina K. and Shaw
775 S. (2017) Uranium(V) Incorporation Mechanisms and Stability in Fe(II)/Fe(III)
776 (oxyhydr)Oxides. *Environ. Sci. Technol. Lett.* **4**, 421–426.

777 Rolison J. M., Stirling C. H., Middag R. and Rijkenberg M. J. A. (2017) Uranium stable isotope
778 fractionation in the Black Sea: Modern calibration of the 238U/235U paleo-redox proxy.
779 *Geochim. Cosmochim. Acta* **203**, 69–88.

780 Romaniello S. J., Herrmann A. D. and Anbar A. D. (2013) Uranium concentrations and
781 238U/235U isotope ratios in modern carbonates from the Bahamas: Assessing a novel
782 paleoredox proxy. *Chem. Geol.* **362**, 305–316.

783 Sahoo S. K., Planavsky N. J., Jiang G., Kendall B., Owens J. D., Wang X., Shi X., Anbar A. D.
784 and Lyons T. W. (2016) Oceanic oxygenation events in the anoxic Ediacaran ocean.
785 *Geobiology* **14**, 457–468.

786 Smit M. A. and Mezger K. (2017) Earth's early O2 cycle suppressed by primitive continents.
787 *Nat. Geosci.* **10**, 788–792.

788 Sperling E. A., Halverson G. P., Knoll A. H., MacDonald F. A. and Johnston D. T. (2013) A
789 basin redox transect at the dawn of animal life. *Earth Planet. Sci. Lett.* **371**–**372**, 143–155.

790 Sperling E. A., Wolock C. J., Morgan A. S., Gill B. C., Kunzmann M., Halverson G. P.,
791 Macdonald F. A., Knoll A. H. and Johnston D. T. (2015) Statistical analysis of iron
792 geochemical data suggests limited late Proterozoic oxygenation. *Nature* **523**, 451–454.

793 Stirling C. H., Andersen M. B., Potter E. K. and Halliday A. N. (2007) Low-temperature isotopic
794 fractionation of uranium. *Earth Planet. Sci. Lett.* **264**, 208–225.

795 Stirling C. H., Andersen M. B., Warthmann R. and Halliday A. N. (2015) Isotope fractionation
796 of 238U and 235U during biologically-mediated uranium reduction. *Geochim. Cosmochim.*
797 *Acta* **163**, 200–218. Available at:
798 http://linkinghub.elsevier.com/retrieve/pii/S0016703715001593.

799 Stylo M., Neubert N., Wang Y., Monga N., Romaniello S. J., Weyer S. and Bernier-Latmani R.
800 (2015) Uranium isotopes fingerprint biotic reduction. *Proc. Natl. Acad. Sci. U. S. A.* **112**,
801 5619–24.

802 Taylor S. R. and McLennan S. M. (1985) *The continental crust: Its composition and evolution*.,
803 Blackwell Scientific, Oxford.

804 Tribovillard N., Algeo T. J., Lyons T. and Riboulleau A. (2006) Trace metals as paleoredox and
805 paleoproductivity proxies: An update. *Chem. Geol.* **232**, 12–32.

806 Wallace M. W., Hood A., Shuster A., Greig A., Planavsky N. J. and Reed C. P. (2017)
807 Oxygenation history of the Neoproterozoic to early Phanerozoic and the rise of land plants.
808 *Earth Planet. Sci. Lett.* **466**, 12–19.

Wang W., Dang D. H., Novotnik B., Phan T. T. and Evans R. D. (2019) Variations in U concentrations and isotope signatures in two Canadian lakes impacted by U mining: A combination of anthropogenic and biogeochemical processes. *Chem. Geol.* **506**, 58–67.

Wang X., Ossa Ossa F., Hofmann A., Agangi A., Paprika D. and Planavsky N. J. (2020) Uranium isotope evidence for Mesoarchean biological oxygen production in shallow marine and continental settings. *Earth Planet. Sci. Lett.* **551**, 116583.

Wang X., Planavsky N. J., Hofmann A., Saupe E. E., De Corte B. P., Philippot P., LaLonde S. V., Jemison N. E., Zou H., Ossa Ossa F., Rybacki K., Alfimova N., Larson M. J., Tsikos H., Fralick P. W., Johnson T. M., Knudsen A. C., Reinhard C. T. and Konhauser K. O. (2018) A Mesoarchean Shift in Uranium Isotope Systematics. *Geochim. Cosmochim. Acta* **238**, 438–452.

Wei W., Frei R., Klaebe R., Tang D., Wei G. Y., Li D., Tian L. L., Huang F. and Ling H. F. (2021) A transient swing to higher oxygen levels in the atmosphere and oceans at ~1.4 Ga. *Precambrian Res.* **354**, 106058.

Weyer S., Anbar a. D., Gerdes a., Gordon G. W., Algeo T. J. and Boyle E. a. (2008) Natural fractionation of 238U/235U. *Geochim. Cosmochim. Acta* **72**, 345–359.

Wood R. and Erwin D. H. (2018) Innovation not recovery: dynamic redox promotes metazoan radiations. *Biol. Rev.* **93**, 863–873.

Xiao S. and Laflamme M. (2009) On the eve of animal radiation: phylogeny, ecology and evolution of the Ediacara biota. *Trends Ecol. Evol.* **24**, 31–40.

Xiao S. and Tang Q. (2018) After the boring billion and before the freezing millions: evolutionary patterns and innovations in the Tonian Period. *Emerg. Top. Life Sci.* **2**, 161–171.

Xu G., Hannah J. L., Bingen B., Georgiev S. and Stein H. J. (2012) Digestion methods for trace element measurements in shales: Paleoredox proxies examined. *Chem. Geol.* **324–325**, 132–147.

Yang S., Kendall B., Lu X., Zhang F. and Zheng W. (2017) Uranium isotope compositions of mid-Proterozoic black shales: Evidence for an episode of increased ocean oxygenation at 1.36 Ga and evaluation of the effect of post-depositional hydrothermal fluid flow. *Precambrian Res.* **298**, 187–201.

Zhang F., Lenton T. M., del Rey Á., Romaniello S. J., Chen X., Planavsky N. J., Clarkson M. O., Dahl T. W., Lau K. V., Wang W., Li Z., Zhao M., Isson T., Algeo T. J. and Anbar A. D. (2020) Uranium isotopes in marine carbonates as a global ocean paleoredox proxy: A critical review. *Geochim. Cosmochim. Acta* **287**, 27–49.

Zhang S., Wang X., Wang H., Bjerrum C. J., Hammarlund E. U., Costa M. M., Connelly J. N., Zhang B., Su J. and Canfield D. E. (2016) Sufficient oxygen for animal respiration 1,400 million years ago. *Proc. Natl. Acad. Sci.* **113**, 1731–1736.

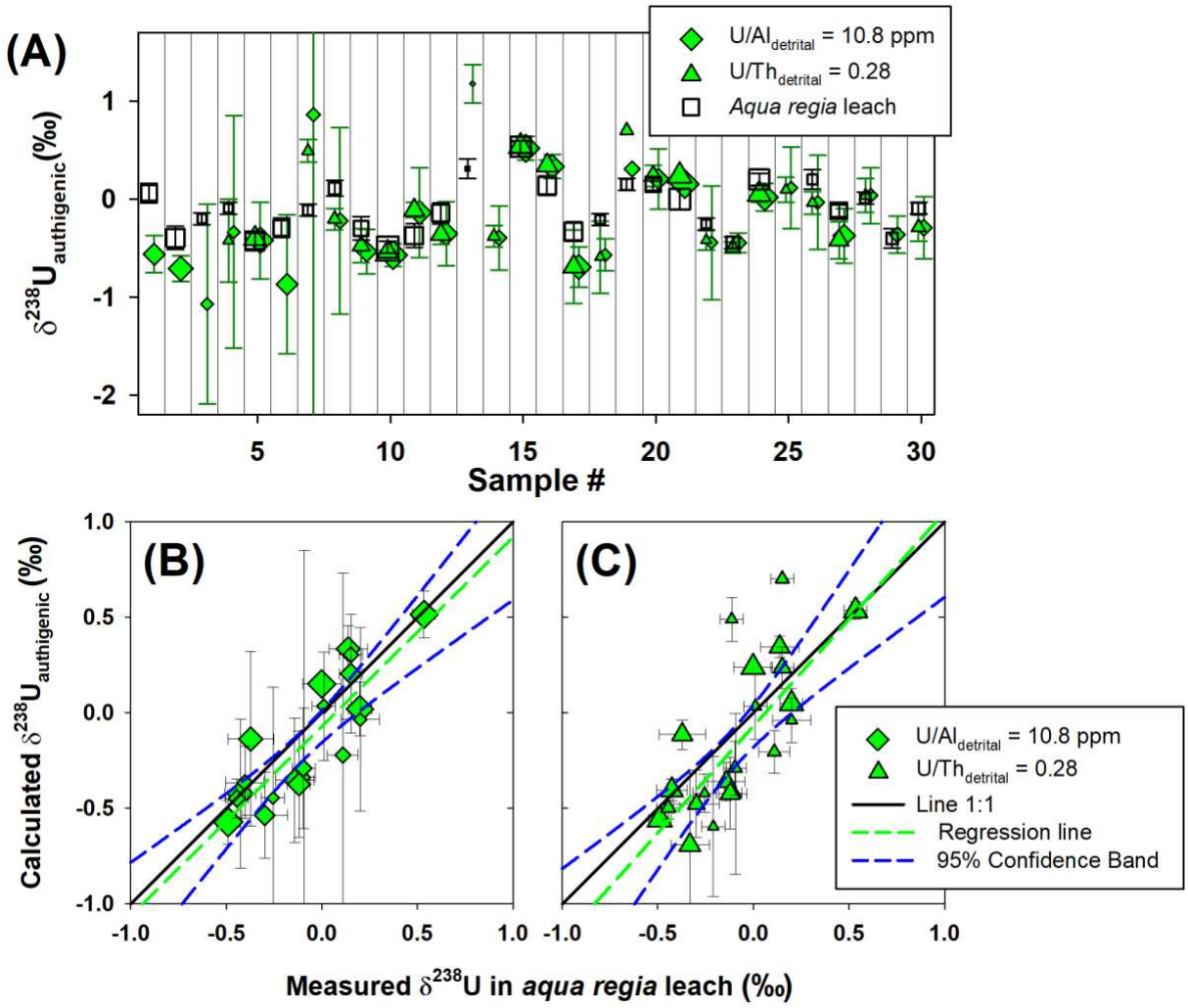

848

849 **Fig. 1:** (A) Comparison of authigenic $\delta^{238}U$ in *aqua regia* extraction methods (white symbols) and
850 determined by the empirical approach using a fixed detrital U/Al ratio (10.8, diamonds) and U/Th
851 ratio (0.28, triangles) in samples of this study. **(B)** and **(C)** panels show biplots of calculated
852 authigenic $\delta^{238}U$ using the U/Al ratio and U/Th ratios, respectively, vs. measured authigenic $\delta^{238}U$
853 in *aqua regia* leaching method. For all panels, the symbol sizes are proportional to total or
854 extracted U concentrations. This and following figures, measurement errors are not shown to
855 enhance readability, but the errors are provided in Supplementary Data 1 and 2.

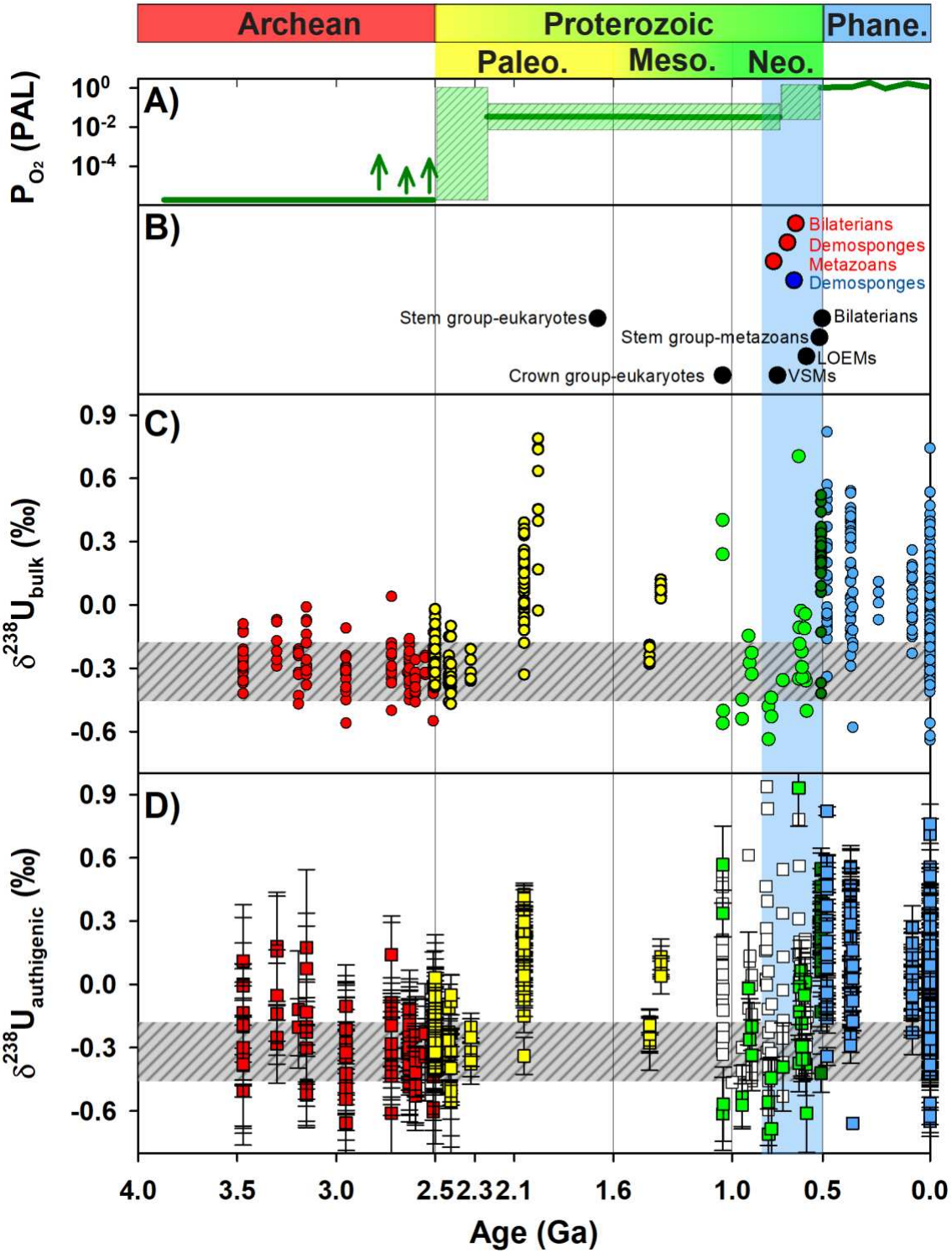

856

857 **Fig. 2:** Summary of shale-hosted U isotope data relative to the evolution of atmospheric O_2 and
858 events in biological evolution. (A) Evolution of atmospheric O_2 through time with a classical two-

859 step (dark green lines) vs. an emerging model (green areas), figure adapted from Lyons et al. (
860 2014). Arrows mark potential Archean "oxygen oases". (B) Summary of major events in biological
861 evolution. Figure adapted from Planavsky et al. (2014) with approximate dates for the first
862 appearance of main eukaryotic groups, obtained using body fossil (red circles), molecular fossil
863 (blue circle) or molecular clock techniques (black circles). (C) Summary of bulk U isotope data in
864 whole rock digestion from published literature on shale samples (circles, red: Archean, yellow:
865 Paleoproterozoic, dark green: late Neoproterozoic, blue: Phanerozoic; see data and references in
866 Supplementary Data 2) and this study (green circles). (D) Authigenic U isotope calculated from
867 the literature (squares using same color code as in C) and this study calculated using a fixed detrital
868 U/Al ratio (green squares) or in *aqua regia* leachates (white squares). Data used for the figure with
869 references are available in Supplementary Data S2. The grey horizontal dashed zone indicates U
870 isotope composition in the average upper crust (-0.31±0.14 ‰; Kendall et al., 2013). The blue area
871 shows the timing of Great Oxidation Event (GOE; Bekker et al., 2004) and the divergence of major
872 eukaryotic clades prior to the Cambrian explosion (Erwin et al., 2011). Error bars on U isotope
873 composition of whole-rocks are not shown to enhance readability; only errors associated with
874 empirical calculations of authigenic $\delta^{238}U$ are shown in panel D. Abbreviations: Paleo.:
875 Paleoproterozoic, Meso.: Mesoproterozoic, Neo.: Neoproterozoic, Phane.: Phanerozoic, LOEMs:
876 Large ornamented Ediacaran microfossils. VSMs: Vased-shaped microfossils.

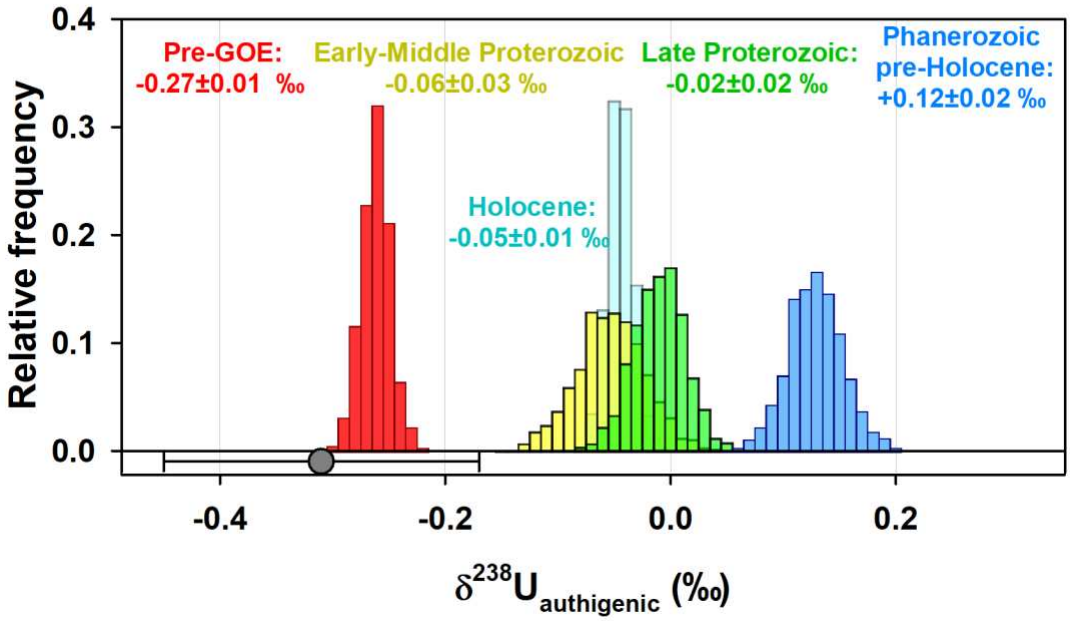

877

878 **Fig. 3:** Bootstrapped means and standard deviations of means generated from 854 authigenic U
879 isotope data (empirically calculated or in *aqua regia* leachates). The bulk U isotope composition
880 of the average upper crust is indicated by the grey circle.

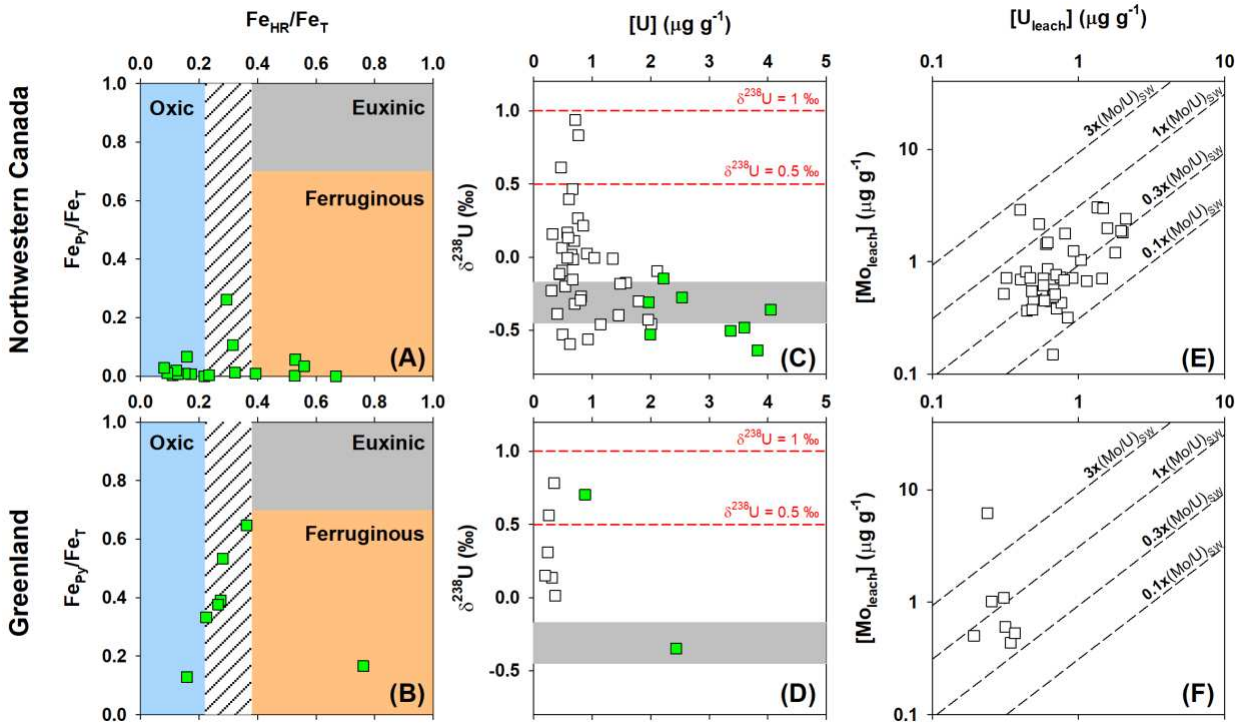

881

882 **Fig. 4:** Geochemical data of the samples from northwestern Canada and Greenland. Data in *aqua*
883 *regia* leach (open squares) and whole-rock digestion (green squares) of marine shales are shown.
884 (A, B) Iron speciation data (Kunzmann et al., 2017b; Gibson et al., 2020), which distinguishes
885 between oxic, ferruginous and euxinic conditions. (C, D) Biplots of U isotope compositions vs. U
886 concentration. The U isotope composition of the average upper crust is indicated by the grey
887 dashed zone. (E, F) Biplot of Mo vs. U in the *aqua regia* selective extraction. The diagonal dashed
888 lines represent the modern seawater (SW) Mo/U weight ratio (3.1) and fractions thereof, according
889 to Algeo and Tribovillard, (2009b).

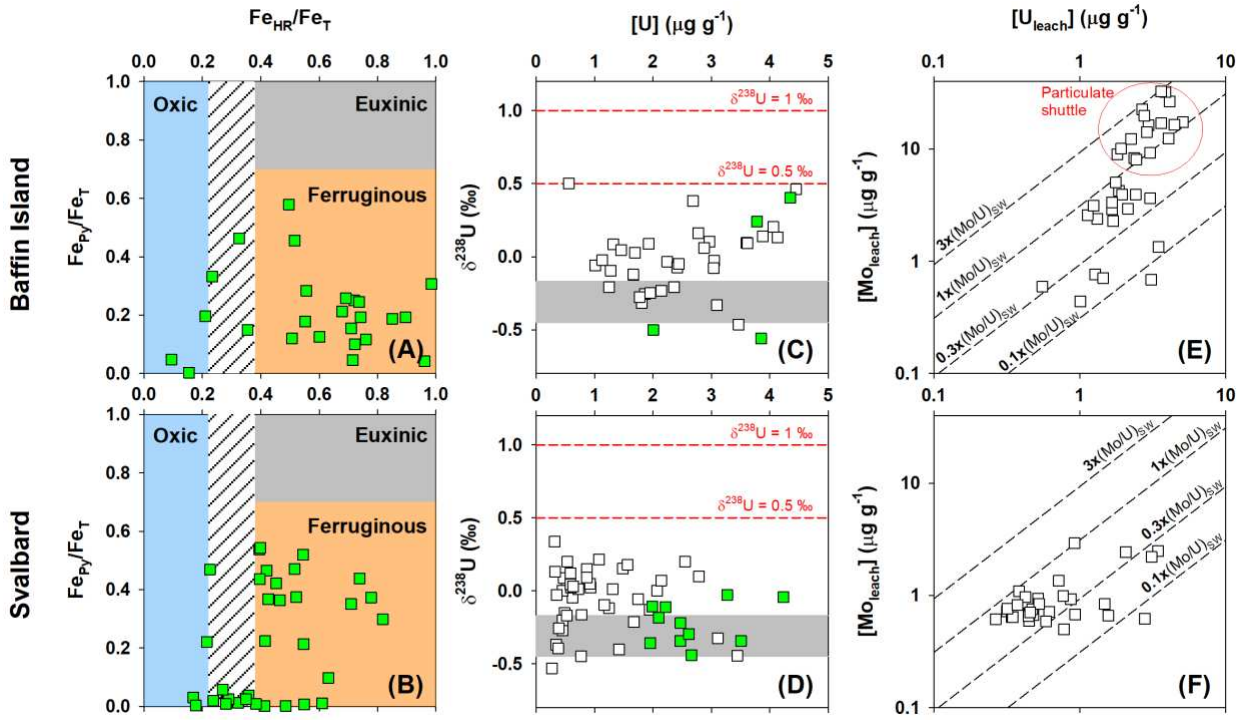

890

891 **Fig. 5:** Geochemical data of the samples from Baffin Island and Svalbard. Data in *aqua regia* leach
892 (open squares) and whole-rock digestion (green squares) of marine shales are shown. (A, B) Iron
893 speciation (Hodgskiss et al., 2020) enabling distinction between oxic, ferruginous and euxinic
894 conditions. (C, D) Biplots of U isotope compositions vs. U concentration. The U isotope
895 composition of the average upper crust is indicated by the grey dashed zone. (E, F) Biplot of Mo
896 vs. U in the *aqua regia* selective extraction. The diagonal dashed lines represent the modern
897 seawater (SW) Mo/U sweight ratio (3.1) and fractions thereof, according to Algeo and
898 Tribovillard, (2009a).

899